Hindawi
Advances in Condensed Matter Physics
Volume 2022, Article ID 9535932, 7 pages
https://doi.org/10.1155/2022/9535932

Research Article

Comparative Study on the Crystallite Size and Bandgap of Perovskite by Diverse Methods

Mohammad Tanvir Ahmed, Shariful Islam, and Farid Ahmed

Department of Physics, Janangirnagar University, Dhaka 1342, Bangladesh

Correspondence should be addressed to Mohammad Tanvir Ahmed; tanvir.phy43@gmail.com

Received 21 January 2022; Revised 24 February 2022; Accepted 2 April 2022; Published 17 May 2022

Academic Editor: Maheswar Nayak

This research demonstrates the fast synthesis of $CH_3NH_3PbBr_3$ perovskite powder via antisolvent addition and further thin-film synthesis by one-step spin coating. The structural and optical properties are investigated via X-ray diffraction, Fourier-transform infrared spectroscopy, and UV–Vis spectroscopy. Crystallite sizes are compared by three different size estimation techniques, which range between 95.8 nm and 105 nm. The perovskite showed a higher absorption coefficient over $10^4\ \mathrm{cm}^{-1}$ and a refractive index from 3.4 to 2.3 in the visible spectrum. The bandgap was estimated via three district methods, which revealed a very slightly varied bandgap in the range of 2.29 eV–2.32 eV.

1. Introduction

Organic-inorganic (OI) perovskites have become a common choice in the research of various optoelectronic (OE) fields. The general formula of OI perovskites is ABX_3, with A, B, and X representing organic cation, metal cation, and halide ion. The enhanced OE properties, abundance of materials, and easy synthesis process made ABX_3 very popular for numerous applications [1, 2]. OI perovskites have shown remarkable success in 3rd generation photovoltaic research, attaining over 25.5% power conversion efficiency [3]. Perovskite materials can offer higher absorption coefficients, broader absorption spectra, higher carrier mobility, longer diffusive lengths, and tunable bandgaps [3]; hence, they are very potential materials for numerous OE applications.

Bromide and iodide-based perovskites are most popular due to their higher absorption coefficient and preferable bandgaps in the visible region. However, $CH_3NH_3PbBr_3$ perovskites are an outstanding compromise between the bandgap and better thermodynamic stability [4], which is an advantage in optoelectronic research over other OI perovskites.

Weber et al. successfully studied the different compositions of the three-dimensional $CH_3NH_3PbX_3$ perovskite material by modifying its crystal structure [5]. They have demonstrated three distinct phases of $CH_3NH_3PbBr_3$ (i.e., cubic, tetragonal, and orthorhombic) and the dependency of lattice parameters on temperature. Schmidt et al. synthesized nanosized $CH_3NH_3PbBr_3$ perovskites using NH_4Br, keeping the nanoparticles dispersed in various solvents [6]. The fast growth of perovskite crystals can be performed via the addition of the antisolvent with the precursor [7], which allows rapid growth of microcrystals or nanocrystals in a short time. Zheng et al. synthesized nanoplatelets of $CH_3NH_3PbBr_3$ using chlorobenzene as the antisolvent, which revealed a higher quantum yield of photoluminescence and a higher decay time [8].

Both the optical and electrical properties of materials are dependent on the synthesis method, the structure of the material, particle size, etc. The estimated particle size and bandgap also depend on the methods of calculation.

The most common method of perovskite synthesis is via evaporation of a precursor solution at low temperatures [9]. For thin-film preparation, various methods such as sol-gel spin coating, microwave-assisted methods, dip coating, spray pyrolysis, and physical vapour deposition have been developed [10]. Among them, the spin coating method is more desirable for perovskite film synthesis due to its high film coverage and low cost [11].

To estimate the average crystallite size from XRD, the Debye–Scherrer (DS) method, the Williamson–Hall (WH) method, and the Halder–Wagner (HW) method can be used [12]. Similarly, bandgaps can be studied via several methods, such as the Tauc method, the Kubelka–Munk (KM) relation, photoluminescence (PL) spectroscopy, and temperature-resistivity relation [13–17].

Here, we report the fast synthesis of methylamine lead bromide (MAPB) perovskites via the addition of the anti-solvent. Structural, optical, and electrical properties of MAPB have been reported. A comparative study of the crystallite size and optical bandgap via different methods has also been performed.

2. Experimental Section

2.1. MAPB Synthesis. The materials used in the synthesis process of MAPB are methylamine (MA) solution 33 wt %, diethyl ether (DE), $PbBr_2$ 99%, hydrobromic acid (HBr) 48%, N,N dimethylformamide (DMF), and toluene.

MA and HBr were reacted at 1 : 1 molar ratio in an ice bath under the temperature of 0°C. After 20 minutes of stirring, the mixture was heated and white MABr crystals were obtained, which were washed several times with DE for removing impurities. MABr and $PbBr_2$ were dissolved in DMF at 1 : 1 ratio to prepare a 0.027 M MAPB solution. The pH and viscosity of the solution were about 5.6 and 1.35 mPa-s. The pH was measured as quickly as possible since DMF dissolves the plastic of the pH sensor. The solution was added dropwise in toluene with continuous stirring. The orange MAPB powder was precipitated, which was then collected via centrifugation. X-ray diffraction was immediately performed on the powder and, later, it was spin coated on a glass substrate for optical characterization. For electrical characterization, a thin disc of MAPB powder was prepared. Figure 1 shows the prepared MAPB powder and thin film.

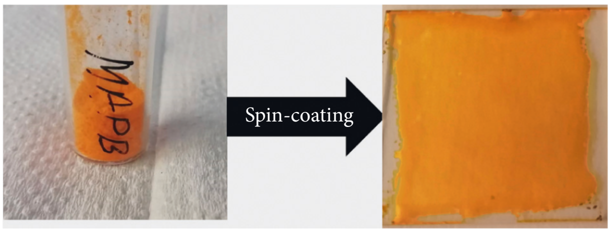

FIGURE 1: Powder and thin film of MAPB perovskite.

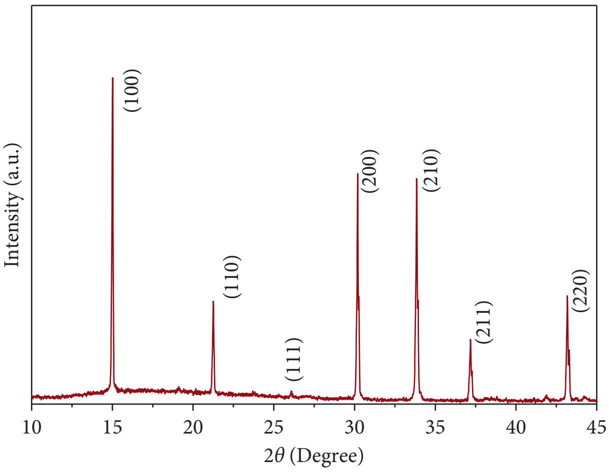

FIGURE 2: XRD spectra of the MAPB powder.

2.2. Characterization. The X-ray diffraction (XRD) and Fourier-transform infrared (FTIR) spectroscopy analyses were performed for all the prepared samples via an Explorer diffractometer and IRPrestige-21, respectively. UV-Vis spectroscopy and Wayne Kerr 6500B Impedance Analyzer were used for analyzing optical and electrical properties.

3. Results and Discussion

3.1. XRD Analysis. The XRD peaks of the prepared MAPB powder were observed at 2θ values of 15.01°, 21.25°, 26.10°, 30.16°, 33.85°, 37.18°, and 43.19° (Figure 2), corresponding to (100), (110), (111), (200), (210), (211), and (220) planes, respectively [18]. The prepared MAPB powder showed fine crystallinity with high periodicity along the (100) direction. The MAPB powder was calculated to be in the cubic phase with a lattice parameter of $a = 5.93076$ Å. The average crystallite was calculated from the DS equation [19, 20]:

$$D_{\mathrm{DS}} = \frac{k\lambda}{\Gamma_s \cos\theta}, \tag{1}$$

where D_{DS}, k, λ, and Γ_s are the crystallite size, Scherrer constant (0.9), X-ray wavelength, and full-width half maxima, respectively. The average crystallite size obtained from the DS method is 95.8 nm. Williamson–Hall (WH) analysis is another simplified method to determine the average crystallite size from peak broadening [19]. According to the WH method, the X-ray diffraction peak widens due to the size and microstrain. The overall broadening may be expressed as follows:

$$\Gamma_s \cos\theta = \frac{k\lambda}{D_{\mathrm{WH}}} + 4\xi \sin\theta, \tag{2}$$

where D_{WH} and ξ are the average crystallite size (measured by WH method) and microstrain, respectively. The intercept of the 4 $\sin\theta$ vs. $\Gamma_s \cos\theta$ plot (Figure 3) is used for D_{WH} estimation. On the other hand, according to the Halder–Wagner (HW) method, the relation between the microstrain, the crystallite size (D_{HW}), and Γ_s can be written as

$$\left(\frac{\Gamma_s}{\tan\theta}\right)^2 = \frac{k\lambda}{D_{\mathrm{HW}}}\,\frac{\Gamma_s}{\tan\theta\,\sin\theta} + 16\xi^2. \tag{3}$$

Hence, in this case, the slope of $\Gamma_s/\tan\theta\sin\theta$ vs. $(\Gamma_s/\tan\theta)^2$ plot (Figure 3) will determine D_{HW}. The average crystallite sizes obtained by DS, WH, and HW methods are 95.8 nm, 103.5 nm, and 105 nm, respectively.

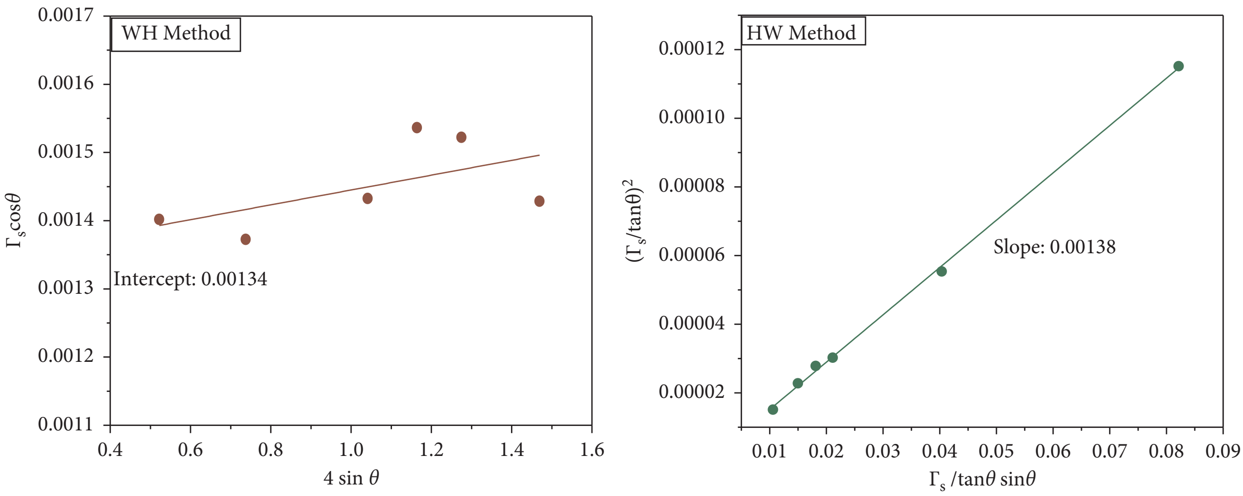

Figure 3: Crystallite size estimation via WH and HW methods.

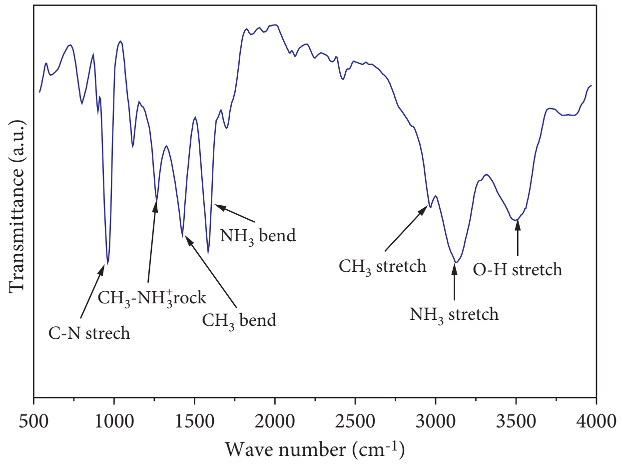

Figure 4: FTIR spectra of the MAPB perovskite.

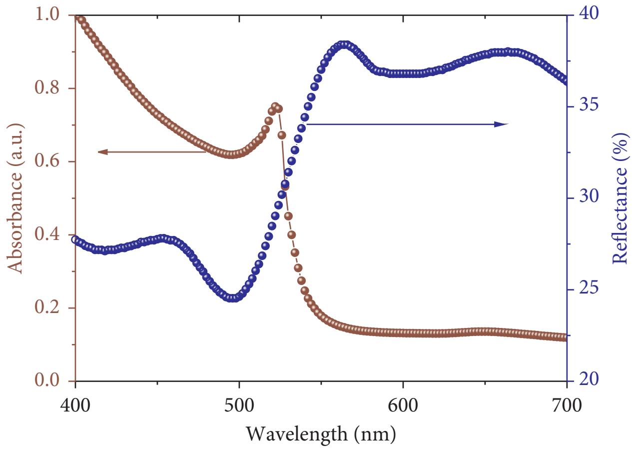

Figure 5: Absorbance and reflectance spectra of the MAPB thin film.

3.2. Vibrational Modes. The FTIR spectra (Figure 4) of the MAPB perovskite show various modes of vibration present in MAPB. C-N stretching, C-H_3 bending, NH_3 bending, CH_3-NH_3 rocking, C-H stretching, and N-H stretching vibrations r identified from the peaks at 960 cm^{-1}, 1426 cm^{-1}, 1584 cm^{-1}, 1260 cm^{-1}, 2965 cm^{-1}, and 3131 cm^{-1}, respectively [21, 22]. However, no peaks of Pb-Br vibrations have been identified since PbX_2 is transparent in IR radiation [23]. The O-H stretching peak represents the presence of moisture in the MAPB sample.

3.3. Optical Properties. The absorbance (A) and reflectance (R) spectra of MAPB were studied in the wavelength range 400 nm–700 nm (Figure 5). The prepared MAPB sample showed higher absorption of the visible spectrum at a shorter wavelength range with an absorption peak at 523 nm [24]. The absorption spectrum shows a sharp absorption edge and very low absorbance in the longer wavelength region of the visible spectrum [4]. Higher reflectance, about 36%, was observed in the longer wavelength region, which signifies the percentage of incident energy loss via reflection. At lower wavelength, the reflectance is comparatively low. The variation of reflectance with the incident wavelength is quite similar to the previous report [25]. Due to low temperature (<150°C), MAPB possessed a higher structural disorder [4]; as a result, crystallite size reduced up to the nanoparticle dimension as obtained from the XRD analysis.

The absorption coefficient and skin depth can be calculated from the following equations [26]:

$$\alpha = 2.303\frac{A}{t}, \qquad \delta = \frac{1}{\alpha}, \tag{4}$$

where α, δ, A, and t represent absorption coefficient, skin depth, absorbance, and film thickness, respectively. Figure 6 shows that a of MAPB is the order of $10^4\ cm^{-1}$, very preferable for OE applications. In the visible region, the absorption coefficient's maximum value is about $2.33 \times 10^4\ cm^{-1}$, with an analogous skin depth of 0.04 μm, whereas at 700 nm, a is $0.26 \times 10^4\ cm^{-1}$ which corresponds to 0.364 μm skin depth.

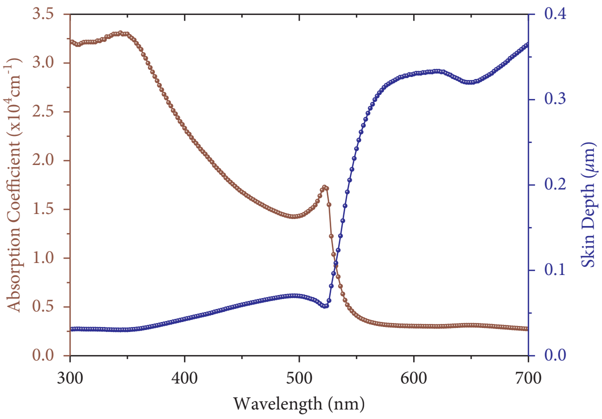

Figure 6: Absorption coefficient and skin depth of the prepared MAPB thin film.

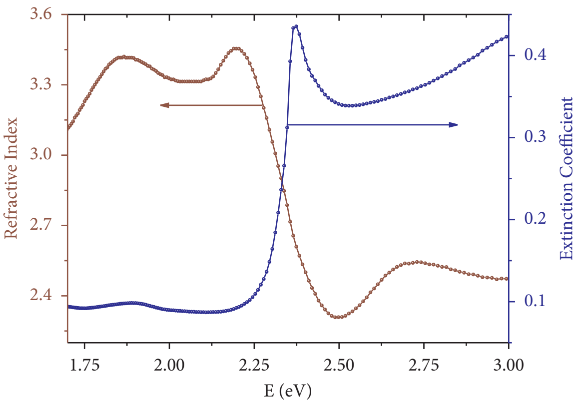

Figure 7: Refractive index and extinction coefficient of the MAPB thin film.

Hence, a few micron thick film is sufficient for absorbing most of the visible spectrum. The decrease in the crystallite size increases the dislocations; as a result, the percentage of voids increases. The increase in voids corresponds to a lower absorption coefficient, i.e., higher skin depth [27]. Hence, the skin depth can be reduced through increasing crystallinity.

The refractive index (η) and extinction coefficient (K) were obtained from the following set of equations [26]:

$$\eta = \frac{1+R}{1-R} + \sqrt{\frac{4R}{(1-R)^2} - K^2},$$
$$K = \frac{\alpha\lambda}{4\pi}, \tag{5}$$

where λ and R are the wavelength and reflectance, respectively; a higher refractive index corresponds to higher reflectivity, whereas the extinction coefficient (K) is the amount of light lost due to absorption or scattering per unit volume of a material. The material possesses a higher refractive index in the lower energy region and a higher extinction coefficient in the higher energy region of the visible spectrum. The maximum refractive index observed was around 2.2 eV energy, about 3.45 (Figure 7). The lower refractive index represents lower crystalline quality [28]. The refractive index can be increased to a higher value via increasing the crystallite size [27]. The peak of the extinction coefficient was near 2.37 eV. Since the extinction coefficient is proportional to the absorption coefficient, K can also be increased by increasing crystallinity.

The optical conductivity (OC) represents the rise in conduction electrons in the presence of photons. OC was calculated from the following equation [29]:

$$\mathrm{OC} = \frac{\alpha\eta C}{4\pi}, \tag{6}$$

where C represents the speed of light. Figure 8 shows that the OC of MAPB is very high in the higher energy regions with a strong peak at 2.37 eV and significantly lower in the low energy regions, which signifies the presence of higher electron density in the conduction band at higher energy absorption [29]. The OC is also a tunable property via maintaining the void percentage. An increase in voids can trap generated carriers. The overall optical conductivity of MAPB was very high, of the order of $10^{14}\,\mathrm{s}^{-1}$.

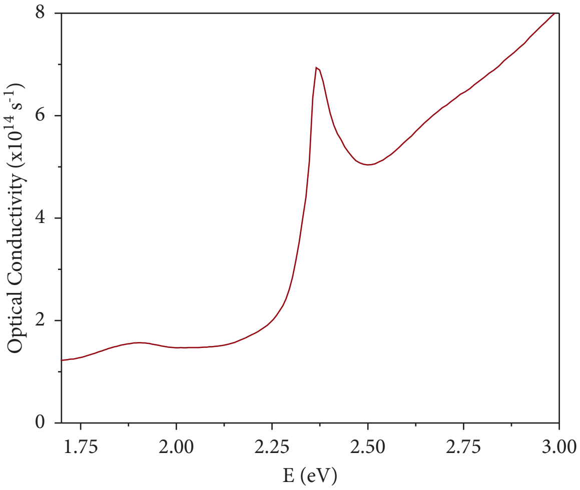

Figure 8: Optical conductivity of the prepared MAPB thin film.

The direct bandgap (E_g) of MAPB was measured in both the Tauc method and KM method. From the Tauc method [30], where the bandgap is measured from the absorbance data, $E_{gA} = 2.32$ eV and, in the KM method, reflectance data were used to obtain the bandgap, which revealed $E_{gR} = 2.29$ eV (Figure 9). A slight variation was observed in the measured bandgap via different methods. The bandgaps are in good agreement with the previous report [27]. It is possible to tune the bandgap of MAPB via modifying the crystallite size since the nanoscale bandgap increases with decreasing crystallite size [31].

UV-Vis spectrometers usually generate absorbance (A) data from the transmittance (T) data through the Beer–Lambert law given by the following equation (7) [32]:

$$A = -\log(T). \tag{7}$$

Although $A + R + T = 1$ in theory, the spectrometer entirely ignores incident wave reflection when determining A. As a result, an exact value of absorbance cannot be achieved, resulting in some departure from correct readings.

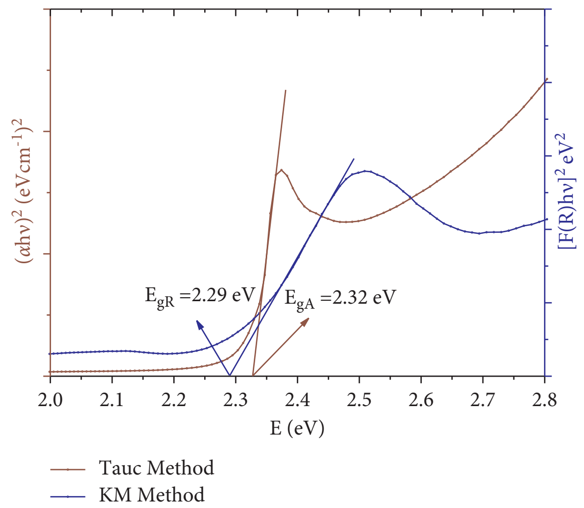

FIGURE 9: Bandgap estimation via the Tauc and KM method.

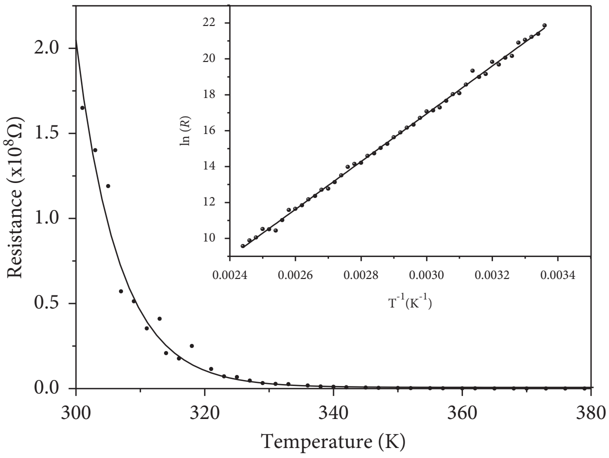

FIGURE 10: Resistance variation of MAPB with temperature.

On the other hand, the KM method for bandgap calculation holds good if the film is thick or shows poor absorption. Since the prepared film showed higher absorbance, the result shows a slight fluctuation and the obtained bandgap showed a certain deviation from the ones calculated via the earlier method.

3.4. Electrical Properties. The negative temperature coefficient of resistance (TCR) caused to decrease in the resistivity of MAPB with increasing temperature. The fitted plot showed an exponential variation of resistance of MAPB with temperature. According to the band theory of solids, the relation between temperature and resistance can be written as follows:

$$R_T = R_P e^{E_{gE}/2k_B T}, \tag{8}$$

where E_{gE}, k_B, T, and R_T represent the energy gap between the top of the valance band and the bottom of the conduction band, Boltzmann constant, Kelvin temperature, and electrical resistance at temperature T, respectively. The above equation can be modified to

$$E_{gE} = 2k_B \frac{\Delta \ln(R)}{\Delta T^{-1}}. \tag{9}$$

From the slope (13307.17) of the plot T^{-1} vs. $\ln(R)$ (Figure 10), the bandgap was calculated to be 2.296 eV, which is quite similar to the ones from previous methods. In the study, copper (Cu) metal was employed as the carrier conduction medium and electrodes. The resistance of Cu rose with temperature due to its metallic behavior, i.e., positive TCR, but the resistance of MAPI dropped with rising temperature. This phenomenon can generate an opposite effect on the carrier conduction through the system, causing a fluctuation in the resistance measurement, resulting in a bandgap deviation. The electrical resistance of the prepared sample depends on the crystallite/grain size. With decreasing crystallite size, the grain boundary per unit volume increases, which reduces the cross transport of charge carriers [33, 34]. Hence, the resistance increases with decreasing crystallinity.

4. Conclusion

The crystalline powder of MAPB perovskite was synthesized successfully via the addition of toluene as an antisolvent. The average crystallite size was calculated via three different methods from XRD spectra, and the obtained size ranged from 95.8 nm to 105 nm. The FTIR spectra verified the presence of different bonds in MAPB. The high absorption coefficient and optical conductivity of 10^4 cm^{-1} and 10^{14} s^{-1} order were obtained, which are highly recommended for various OE applications. Up to 36% reflectance was observed with the refractive index from 3.45 to 2.3 in the visible wavelength region. The bandgap of the MAPB perovskite was measured via different methods (optical and electrical), and a very slight variation was observed. The measured bandgaps ranged from 2.29 eV to 2.32 eV.

Data Availability

The data used to support the findings of this study have not been made available because they are still being used in an ongoing research.

Conflicts of Interest

The authors declare that there are no conflicts of interest regarding the publication of this article.

Acknowledgments

This research has been supported by the Condensed Matter Physics Lab of the Department of Physics, Jahangirnagar University, Dhaka-1342, Bangladesh. The financial support for this research was provided by the National Science and Technology (NST) fellowship under the Ministry of Science and Technology, Bangladesh.

Supplementary Materials

Graphical abstract of the research article. (*Supplementary Materials*)

References

[1] J. Chen, S. Zhou, S. Jin, H. Li, and T. Zhai, "Crystal organometal halide perovskites with promising optoelectronic applications," *Journal of Materials Chemistry C*, vol. 4, no. 1, pp. 11–27, 2015.

[2] A. Maity, S. Mitra, C. Das, S. Siraj, A. K. Raychaudhuri, and B. Ghosh, "Universal sensing of ammonia gas by family of lead halide perovskites based on paper sensors: experiment and molecular dynamics," *Materials Research Bulletin*, vol. 136, Article ID 111142, 2021.

[3] T. Wu, Z. Qin, Y. Wang et al., "The main progress of perovskite solar cells in 2020–2021," *Nano-Micro Letters*, vol. 13, no. 1, pp. 152–218, 2021.

[4] C. Wolf, J. S. Kim, and T. W. Lee, "Structural and thermal disorder of solution-processed CH3NH3PbBr3 hybrid perovskite thin films," *ACS Applied Materials & Interfaces*, vol. 9, no. 12, pp. 10344–10348, 2017.

[5] A. Poglitsch and D. Weber, "Dynamic disorder in methylammoniumtrihalogenoplumbates (II) observed by millimeter-wave spectroscopy," *The Journal of Chemical Physics*, vol. 87, no. 11, pp. 6373–6378, 1987.

[6] L. C. Schmidt, A. Pertegas, S. Gonzalez-Carrero et al., "Nontemplate synthesis of CH3NH3PbBr3 perovskite nanoparticles," *Journal of the American Chemical Society*, vol. 136, no. 3, pp. 850–853, 2014.

[7] S. Pathak, N. Sakai, F. Wisnivesky Rocca Rivarola et al., "Perovskite crystals for tunable white light emission," *Chemistry of Materials*, vol. 27, no. 23, pp. 8066–8075, 2015.

[8] H. Zheng, W. Pan, and W. Shen, "One-step synthesis of colloidal CH3NH3PbBr3 nanoplatelets via chlorobenzene to realize nonsolvent crystallization," *Nanotechnology*, vol. 29, no. 45, Article ID 455601, 2018.

[9] S. Arya, P. Mahajan, R. Gupta et al., "A comprehensive review on synthesis and applications of single crystal perovskite halides," *Progress in Solid State Chemistry*, vol. 60, Article ID 100286, 2020.

[10] F. Aslan, G. Adam, P. Stadler, A. Goktas, I. H. Mutlu, and N. S. Sariciftci, "Sol-gel derived In2S3 buffer layers for inverted organic photovoltaic cells," *Solar Energy*, vol. 108, pp. 230–237, 2014.

[11] R. A. Kerner, L. Zhao, Z. Xiao, and B. P. Rand, "Ultrasmooth metal halide perovskite thin films: via sol-gel processing," *Journal of Materials Chemistry*, vol. 4, no. 21, pp. 8308–8315, 2016.

[12] D. Nath, F. Singh, and R. Das, "X-ray diffraction analysis by Williamson-Hall, Halder-Wagner and size-strain plot methods of CdSe nanoparticles- a comparative study," *Materials Chemistry and Physics*, vol. 239, Article ID 122021, 2020.

[13] G. M. Kimball, A. M. Müller, N. S. Lewis, and H. A. Atwater, "Photoluminescence-based measurements of the energy gap and diffusion length of Zn3 P2," *Applied Physics Letters*, vol. 95, no. 11, pp. 112103–112106, 2009.

[14] J. Tauc, *Amorphous and Liquid Semiconductors*, Plenum press, New York, NY, USA, 1974.

[15] B. Ketterer, M. Heiss, M. J. Livrozet, A. Rudolph, E. Reiger, and A. Fontcuberta I Morral, "Determination of the band gap and the split-off band in wurtzite GaAs using Raman and photoluminescence excitation spectroscopy," *Physical Review B*, vol. 83, no. 12, pp. 125307–125316, 2011.

[16] P. Makuła, M. Pacia, and W. Macyk, "How to correctly determine the band gap energy of modified semiconductor photocatalysts based on UV-vis spectra," *Journal of Physical Chemistry Letters*, vol. 9, no. 23, pp. 6814–6817, 2018.

[17] M. Petit, L. Michez, J. M. Raimundo, and P. Dumas, "Electrical and optical measurements of the bandgap energy of a light-emitting diode," *Physics Education*, vol. 51, no. 2, Article ID 25003, 2016.

[18] A. Jaffe, Y. Lin, C. M. Beavers, J. Voss, W. L. Mao, and H. I. Karunadasa, "High-pressure single-crystal structures of 3D lead-halide hybrid perovskites and pressure effects on their electronic and optical properties," *ACS Central Science*, vol. 2, no. 4, pp. 201–209, 2016.

[19] R. Rai, T. Triloki, and B. K. Singh, "X-ray diffraction line profile analysis of KBr thin films," *Applied Physics A*, vol. 122, no. 8, p. 774, 2016.

[20] K. S. Ahmad, H. Siraj, S. B. Jaffri et al., "Physical vapor deposited [Co:Cd-(dtc)2]/SnO2 dual semiconductor systems: synthesis, characterization and photo-electrochemistry," *Journal of Inorganic and Organometallic Polymers and Materials*, vol. 31, no. 6, pp. 2579–2593, 2021.

[21] T. Glaser, C. Muller, M. Sendner et al., "Infrared spectroscopic study of vibrational modes in methylammonium lead halide perovskites," *Journal of Physical Chemistry Letters*, vol. 6, no. 15, pp. 2913–2918, 2015.

[22] Q. Wang, T. Yang, H. Wang et al., "Morphological and chemical tuning of lead halide perovskite mesocrystals as long-life anode materials in lithium-ion batteries," *CrystEngComm*, vol. 21, no. 6, pp. 1048–1059, 2019.

[23] J. M. C. d. Silva Filho, V. A. Ermakov, and F. C. Marques, "Perovskite thin film synthesised from sputtered lead sulphide," *Scientific Reports*, vol. 8, no. 1, pp. 1563–1568, 2018.

[24] H. Mehdi, A. Mhamdi, R. Hannachi, and A. Bouazizi, "MAPbBr3 perovskite solar cells via a two-step deposition process," *RSC Advances*, vol. 9, no. 23, p. 12906, 2019.

[25] S. Schünemann, K. Chen, S. Brittman, E. Garnett, and H. Tüysüz, "Preparation of organometal halide perovskite photonic crystal films for potential optoelectronic applications," *ACS Applied Materials & Interfaces*, vol. 8, no. 38, pp. 25489–25495, 2016.

[26] R. Suresh, V. Ponnuswamy, R. Mariappan, and N. Senthil Kumar, "Influence of substrate temperature on the properties of CeO2 thin films by simple nebulizer spray pyrolysis technique," *Ceramics International*, vol. 40, no. 1, pp. 437–445, 2014.

[27] M. S. Alias, I. Dursun, M. I. Saidaminov et al., "Optical constants of CH_3NH_3PbBr_3 perovskite thin films measured by spectroscopic ellipsometry," *Optics Express*, vol. 24, no. 15, Article ID 16586, 2016.

[28] A. Tumbul, A. Göktaş, M. Z. Zarbali, and F. Aslan, "Structural, morphological and optical properties of the vacuum-free processed CZTS thin film absorbers," *Materials Research Express*, vol. 5, no. 6, Article ID 066408, 2018.

[29] K. A. Uyanga, S. C. Ezike, A. T. Onyedika, A. B. Kareem, and T. M. Chiroma, "Effect of acetic acid concentration on optical properties of lead acetate based methylammonium lead iodide perovskite thin film," *Optical Materials*, vol. 109, Article ID 110456, 2020.

[30] M. T. Ahmed, S. Islam, and F. Ahmed, "Synthesis of $(CH_3NH_3)_2CuCl_4$ nanoparticles by antisolvent engineering," *Journal of Crystal Growth*, vol. 587, Article ID 126637, 2022.

[31] T. Zahra, K. S. Ahmad, C. Zequine et al., "Semi-conducting Ni/Zn nano-hybrids' driven efficient electro-catalytic performance: fabrication, characterization, and electrochemical features' elucidation," *Green Chemistry Letters and Reviews*, vol. 14, no. 2, pp. 286–301, 2021.

[32] D. F. Swinehart, *Journal of Chemical Education*, vol. 39, no. 7, p. 333, 1962.

[33] M. T. Ahmed, S. Islam, M. S. Bashar, and F. Ahmed, "One-step synthesis of (CH3NH3)2CuCl4:ZnS thin film for optoelectronic applications," *Crystal Research and Technology*, vol. 57, no. 4, Article ID 2100235, 2022.

[34] M. T. Ahmed, S. Islam, M. S. Bashar, M. A. Hossain, and F. Ahmed, "Synthesis and characterizations of CH3NH3PbI3: ZnS microrods for optoelectronic applications," *Advances in Materials Science and Engineering*, vol. 2022, Article ID 7606339, 14 pages, 2022.